Impact of the Polymorphism and Relativistic Effects on the Electronic Properties of Inorganic Metal Halide Perovskites

Luis Octavio de Araujo,* Celso R. C. Rêgo,* W. Wenzel,* Fernando P. Sabino,* and Diego Guedes-Sobrinho*

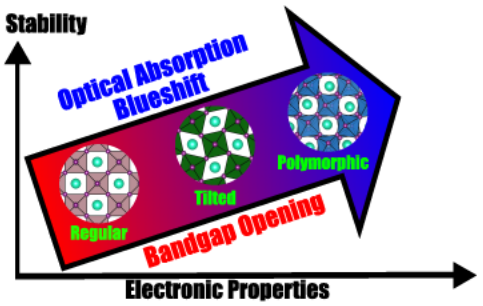

ABSTRACT: Recent finds have revealed in metal halide perovskites the presence of lower local symmetry contributions especially in the cubic phase in detriment to its high symmetry monomorphic structure ($Pm\,3m$). We analyzed the impact of the polymorphic nature in $CsBX_3$ inorganic perovskites (B = Ge, Sn, Pb; X = Cl, Br, I) through first principle calculations to show how the polymorphism contributes more to the material stability than their monomorphic counterparts. Distinct stability trends can be seen for each halogen and metal series, revealing the role of the (strong) spin−orbit coupling (SOC) on the stability throughout the Ge → Sn → Pb sequence from a set of local motif contributions, such as distortions on the octahedrons, relative tiltings, Cs displacement, and metal off centering networks. The combination of relativistic quasiparticle correction and SOC provided accurate values of gap energies, showing that the experimental measurement is actually an average from structural local motif contributions. At the same time, given the absence of a prohibited transition, a blue shift in the UV−vis spectra was observed for all chemical compositions from high symmetry structure → polymorphic version. This result revealed that a high suppression of the total optical absorption can be avoided through the replacement of the toxic Pb by greener alternatives, especially $CsSnX_3$ and $CsGeX_3$ (X = Br and I), providing a potential perspective to the market of solar cell devices.

1. INTRODUCTION

Inorganic metal halide perovskites (MHPs) have emerged in the past few years as low cost alternatives to silicon for the fabrication of solar cells. Because the power conversion efficiencies have exceeded 25% for $FAPbI_3$,[1] inorganic versions with A = Cs in the ABX_3 formula (where B = Pb and X = Cl, Br, and, under proper conditions, I) have stood out for presenting moisture and thermal stability better than that of their hybrid relatives, which could culminate in devices with increased durability.[2] However, the presence of toxic Pb may hinder commercial manufacture, and its substitution by less toxic cations, such as Ge and Sn, is promising. Conversely, both of these elements are known to undergo oxidation from II to IV state, which could lead to faster degradation of the corresponding halide perovskites.[3−5] Nevertheless, optoelectronic properties, such as absorption coefficient, gap energy, and charge carrier lifetimes, are strongly influenced by the chemical composition and its impact on the crystal structure, e.g., through different stable polymorphic contributions.[5−7] Therefore, understanding the correlation between composition, polymorphism, and electronic properties is essential for potential improvements in solar cells involving MHPs.

Recent studies have revealed that the MHP regular cubic phase ($Pm\,3m$ spacegroup) characterized by X ray diffraction (XRD), for instance, ABX_3 (A = Cs, MA, or FA, B = Pb, or Sn, and X = Cl, Br, or I), is a macroscopic average of the material in an atomistic network.[8,9] The crystal is constituted by local motifs in a short space range (a few angstroms) with symmetry lower than that of the regular octahedra in the $Pm\,3m$ structure, which are not captured by XRD due to long coherence length.[8] These local motifs are identified as a set of distortions, such as (i) B metal off center displacements within octahedra,[10] (ii) octahedrons tilts,[8] (iii) positional rearrangements of the A cations within the cuboctahedral cavities, (iv) and Jahn−Teller distortions.[9,11] All of them may coexist in the material's ionic network and confer the optoelectronic properties experimentally measured. However, details about how the set of local motifs affects the electronic properties of MHPs through cooperative effects remain an open question.

Theoretical studies suggest that such structural changes would reduce the system's internal energy, which would lead to an impact on the electronic properties.[9,10] However, it is crucial in theoretical approaches to capture these polymorphism effects into gap energy and optical absorption investigations context. Thus, for approaches based on the density functional theory

(DFT), for instance, the widely used semilocal exchange correlation functionals (as those based on generalized gradient approximation) are known by the large underestimation of the gap energies with respect to the experimental values.[12−14] In inorganic MHPs the exchange correlation failure is even more dramatic when spin−orbit coupling (SOC) effects are included, which yields a calculated gap energy of 0.79 eV for $CsGeI_3$,[15] 0.49 eV for $CsSnI_3$,[16] and 0.63 eV for $CsPbI_3$[17] as models based on the unit cell, while the experimental values are 1.63 eV,[18] 1.30 eV,[3] and 1.73 eV,[19] respectively.

Hybrid functional approaches would be alternatives to solve this gap energy underestimation problem. For instance, employing an exchange correlation functional as proposed by Heyd−Scuseria−Ernzerhof (HSE06),[20,21] a recent study for $CsGeX_3$ (X = Cl, Br, or I) MHPs by using 25% of exact exchange (ex.)[11] provided good results for the distorted unit cell for $CsGeCl_3$ ($CsGeBr_3$), reaching 2.88 eV (2.07 eV) which is close to the 1.93−3.67 eV (1.59−2.32 eV) experimental interval measured from room pressure up to 3.3 GPa (1.2 GPa).[22] Hybrid functionals with high exact ex. percentage (43−45%)[15,23] and GW[24] have provided gap energies for $CsGeI_3$ (1.57 eV, $HSE^{ex.\ 45\%}$+SOC),[15] $CsSnI_3$ (1.01 eV, GW+SOC),[13] and $CsPbI_3$ (1.62 eV, GW+SOC)[25] in better agreement with the experimental reports. However, if for the HSE functional the exact exchange part needs to be tuned, on the other hand, its high computational cost is the Achilles' heel for studies involving polymorphs represented by large supercells, which for GW would be unthinkable.

We investigated the effects of the structural polymorphism on the stability and electronic properties (gap energies and optical absorption) of all inorganic MHPs based on the ABX_3 chemical formula, where A = Cs, B = Ge, Sn, Pb, and X = Cl, Br, I. As an alternative to the hybrid functionals or GW methods, our protocol accounts for the spin−orbit coupling effects combined with the DFT 1/2 relativistic quasiparticle correction,[26] whose computational cost is comparable with the standard DFT. Our results are in excellent agreement regarding the experimental reports, which confirm the impact of the structural poly morphism on the optoelectronic properties on all MHPs chemical compositions addressed here.

2. COMPUTATIONAL DETAILS

Configuration of the Polymorphs. We used a cubic structure based on the cubic unit cell (UC: 1 × 1 × 1), from which the supercells with $\sqrt{2} \times \sqrt{2} \times 2$ (20 atoms) and $2\sqrt{2} \times 2\sqrt{2} \times 2$ (80 atoms) sizes were constructed. From these models three polymorphs were proposed: regular (R), tilted (T), and polymorphic (P) networks, as depicted in Figure 1, from which all inorganic ABX_3 compounds (A = Cs, B = Ge, Sn, Pb, and X = Cl, Br, I) were investigated. It is important to highlight that the unit cell and the R networks were fully optimized geometrically from their atom positions and stress tensor (*Pm* 3*m* symmetry as identified through XRD), wherein only the atomic positions were reoptimized for the construction of the T and P networks. Thus, the $\sqrt{2} \times \sqrt{2} \times 2$ supercell was able to capture the T network for all perovskite compositions, whereas into the $2\sqrt{2} \times 2\sqrt{2} \times 2$ P network all the local motifs aforementioned, such as B metal off centering, Cs displacement into the cavity site, Jahn−Teller distortions, and tilts between octahedrons, are collectively contributing to the system through random displacements from the optimization of the atoms. Representa tive pictures about the polymorphic contributions which can be found in the P networks and Cartesian coordinates of general

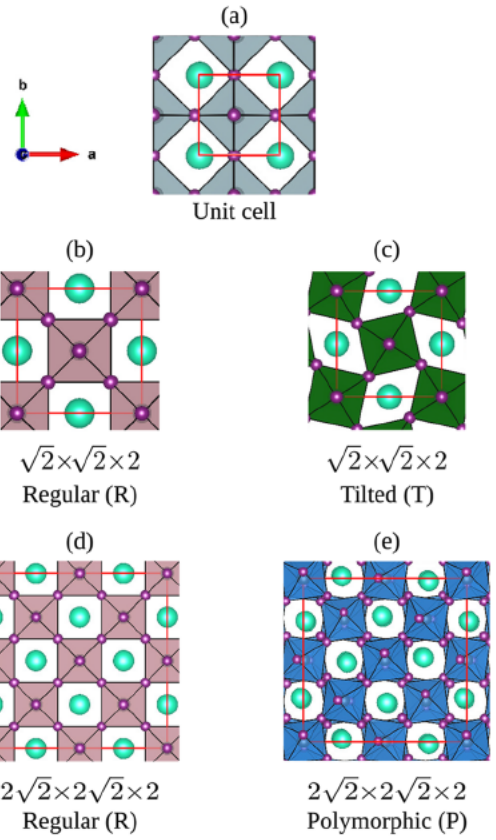

Figure 1. Representation of the cubic structure for $CsBX_3$ inorganic MHP where B = Ge, Sn, or Pb, and X = Cl, Br, or I. (a) Cubic unit cell (UC), (b) $\sqrt{2} \times \sqrt{2} \times 2$ supercell as a regular (R) network, (c) $\sqrt{2} \times \sqrt{2} \times 2$ supercell as a tilted (T) network, (d) $2\sqrt{2} \times 2\sqrt{2} \times 2$ supercell as a regular (R) network, and (e) $2\sqrt{2} \times 2\sqrt{2} \times 2$ supercell as a polymorphic (P) network. The unit cell and supercell edges used are indicated by red lines.

models for UC, R, T, and P are available in Supporting Information (Figure S2 and Tables S5, S6, S7, and S8, respectively).

Total Energy Calculations. All the total energy calculations and structure optimization were DFT based[27,28] within the Perdew−Burke−Ernzerhof (PBE)[29] approach for the exchange correlation functional. To solve the Kohn−Sham (KS) equations, we employed Vienna Ab Initio Simulation Package (VASP code)[30,31] with the projector augmented wave (PAW)[32] method. For the valence electrons, the following configurations were considered: Cs ($5s^2$, $5p^6$, $6s^1$), Pb ($5s^2$, $5d^{10}$, $6s^2$, $6p^2$), Sn ($4d^{10}$, $5s^2$, $5p^2$), Ge ($3d^{10}$, $4s^2$, $4p^2$), Cl ($3s^2$, $3p^5$), Br ($4s^2$, $4p^5$), and I ($5s^2$, $5p^5$). Scalar relativistic effects and spin−orbit coupling (SOC) interactions are present to the core and valence states in all calculations. To integrate over the Brillouin zone of the cubic unit cells, an 8 × 8 × 8 k points mesh was used for the $CsGeBr_3$, $CsGeI_3$, $CsSnI_3$, $CsPbBr_3$, and $CsPbI_3$ compounds, while a 9 × 9 × 9 k points mesh was used for $CsGeCl_3$, $CsSnBr_3$, $CsSnCl_3$, and $CsPbCl_3$. The same k mesh densities were employed to integrate over the Brillouin zone of the supercell configurations. Plane waves were expanded up to a cutoff energy of 430 eV so that the total energy convergence criteria was defined as 1.0×10^{-5} eV, whereas the Hellmann−Feynman forces were relaxed until they were smaller than 0.010 eV $Å^{-1}$ on every atom.

Gap Energy from Relativistic Quasiparticle Correction. We computed the gap energies and optical absorption coefficients via the DFT 1/2 quasiparticle approach.[26] The method is based on Slater's half ion technique, which equals the atomic ionization potential to the negative of the atomic eigenvalue at half occupation.[33,34] For crystals, the DFT 1/2 method uses a modified Kohn–Sham (KS) potential ($V_{mod,KS}(\vec{r})$) to calculate the half occupied eigenvalue of the orbital in the valence band top. This potential is obtained by taking the difference between the self energy potential ($V_S(\vec{r})$) and the standard KS potential ($V_{KS}(\vec{r})$), wherein $V_{mod,KS}(\vec{r}) = V_{KS}(\vec{r}) - V_S(\vec{r})$.[35] The former is approximated by the expression $V_S(\vec{r}) = \Theta(\vec{r},CUT)[V_0(\vec{r}) - V_{-1/2}(\vec{r})]$, in which $V_0(\vec{r})$ and $V_{-1/2}(\vec{r})$ are, respectively, the Kohn–Sham potential for the neutral and half ionized atoms. The $\Theta(\vec{r},CUT)$ step function trims $V_S(\vec{r})$ at the CUT distance by preventing the Coulomb interaction penetration among neighboring atoms, which is determined variationally by maximizing the gap energy free of empirical parameters.[35,36] Details about the CUT optimization procedure are shown in Supporting Information (Figure S1). UV–vis spectra were calculated using imaginary and real parts of the dielectric function, the former calculated within the random phase approximation[37] and the latter obtained via Kramers–Kronig transformation.[9,38] To speed the data acquisition, we have employed the Workflow Active Nodes (WaNo) DFT VASP[39,40] developed within the SimStack workflow framework to manage part of the protocol. The whole protocol requires the submission and monitoring of many sets of simulations for independent tasks in a different geometry. Thus, using a workflow helps us save time by automatizing and reducing the complexity of the protocol, allowing us to focus on the science and not on the procedure.

3. RESULTS AND DISCUSSION

Structural Analysis. The lattice parameters calculated for all perovskites and supercell sizes are shown in Figure 2. The values follow the atomic size increase of metal B and halogen X, that is, $CsGeX_3 < CsSnX_3 < CsPbX_3$ for X = Cl, Br, or I, and $CsBCl_3 < CsBBr_3 < CsBI_3$ for B = Ge, Sn, or Pb. This result is in agreement with the relative difference for ionic sizes with respect to Pb (for the metals) and I (for the halogens), wherein Sn (Ge) is 0.84% (38.66%) smaller than that of Pb, and Br (Cl) is 14.29% (25.56%) smaller than that of I.[46] In comparison with experimental reports,[18,22,41−45] an excellent agreement was found with all percent deviations smaller than 3% in the modulus for the lattice parameters from the unit cell → $\sqrt{2} \times \sqrt{2} \times 2$ ($2\sqrt{2} \times 2\sqrt{2} \times 2$). For instance, the deviations of 2.79%, 1.69%, and 2.17% for $CsGeCl_3$, $CsGeBr_3$, and $CsGeI_3$, respectively, as unit cells reduced to −0.74%, − 0.62%, and 0.17% as $2\sqrt{2} \times 2\sqrt{2} \times 2$ R and P networks. Similar behavior is observed for $CsSnX_3$ and $CsPbX_3$, as detailed in Table S3 in Supporting Information.

We calculated the radial distribution functions $g(r)$ to analyze the octahedral tilts and their distortions for the T and P networks to compare with the high symmetry R network by taking as a reference site the B metal within the octahedra. Figure 3(b–d) shows the $g(r)$ distributions with respect to B for the B–X, B–B, and B–Cs distances, as depicted in panel a. Regular (R) networks are characterized by $g(r)$ profiles with well defined distances pairwise so that the local motif profile is based on platonic octahedrons (archimedean cuboctahedrons) with centrosymmetric B (Cs) at their sites into supercells. On the basis of that, all the R network B–X–B angles lying on 180° (or $a^0a^0a^0$ from Glazer's notation)[47] can be considered as a reference. Octahedral tiltings into T were reached in phase on the *ab* equatorial plane (i.e., $a^0a^0c^+$), whereas P networks were reached predominantly in out phase (e.g., $a^-b^-c^+$) through the random structure optimization procedure. Numerical results related to the BX_3 octahedrons, such as smallest and largest B–X distances, and B–X–B angles for all compositions are presented in Table S2 of Supporting Information.

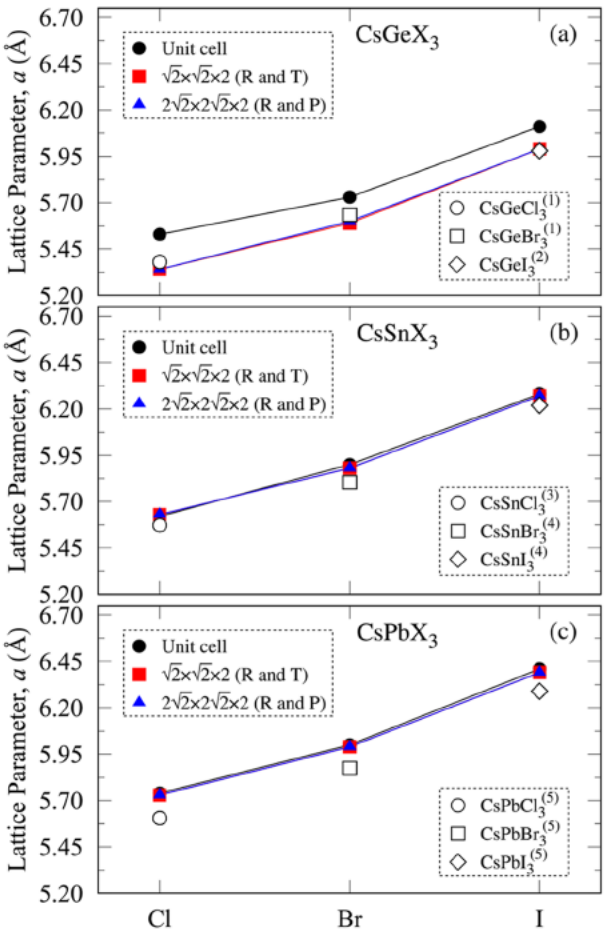

Figure 2. Lattice parameters for all cell sizes of all inorganic cubic halide perovskites for the unit cell, T, and R networks of the (a) $CsGeX_3$, (b) $CsSnX_3$, and (c) $CsPbX_3$ (X = Cl, Br, I) perovskites. Experimental lattice constants: (1) ref 22, (2) ref 18, (3) ref 41, (4) refs 42, 43, (5) refs 44, 45.

$B–X^{(1)}$ distances are indicated by $g(r)$ into the 2.6–3.3 Å interval (dotted rectangle), whereas B–Cs ([111] direction) is highlighted for the solid turquoise rectangles, e.g., $g(r)$ into 5.0–6.0 Å (4.2–5.0 Å) for $CsSnI_3$ or $CsPbI_3$ ($CsGeCl_3$). The B distance for the first neighbors B metal sites (⟨100⟩ directions) lies on the intervals highlighted by black dashed rectangles, whereas second halogen neighbors for $B–X^{(2)}$ (in Figure 3(a)) appear on the last highlighted intervals, e.g., into 7.0–8.0 Å (6.0–7.0 Å) for $CsPbI_3$ ($CsGeCl_3$). One observes in the T network that while the octahedron tiltings depicted by the $g(r)$ splitting into $B–X^{(2)}$ pairwise, $B–X^{(1)}$ pairs forming octahedrons are not affected, i.e., even with octahedron tiltings, the T networks keep their B metal on centering. Conversely, into P networks, all the B metal off center displacements, octahedron tilt, and the Cs rearrangement contributions are indicated

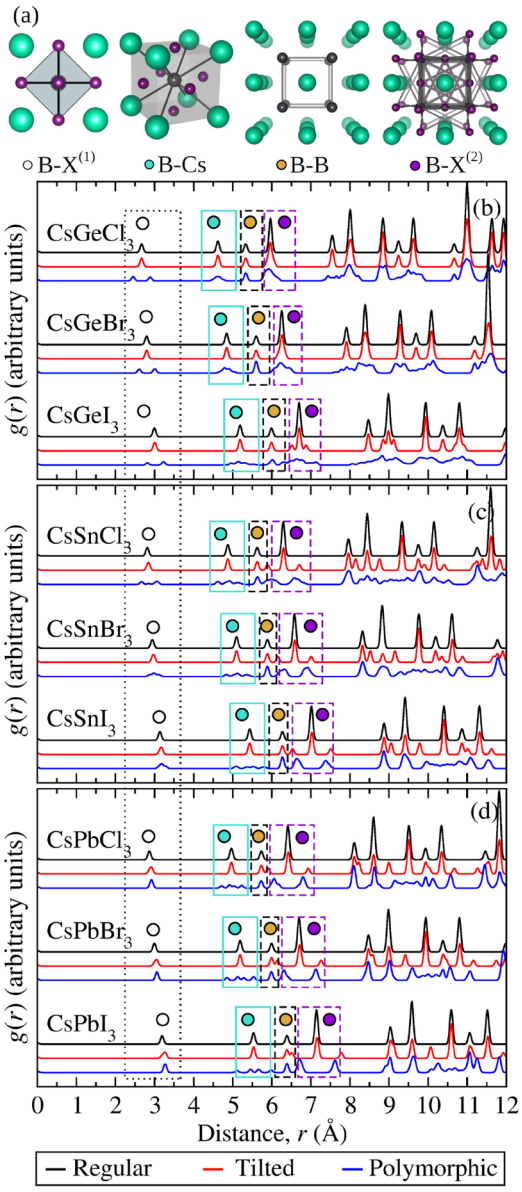

Figure 3. (a) Representations of the pairwise combinations for B–$X^{(1)}$ (first neighbors), B–Cs, B–B, and B–$X^{(2)}$ (second neighbors). Radial distribution functions $g(r)$ for (b–d) all inorganic MHPs from their R ($a^0a^0a^0$), T ($a^0a^0c^+$), and P (e.g., $a^-b^-c^+$) networks. The pairwise combinations are indicated by dotted and dashed rectangles.

through the $g(r)$ splitting and broadening into their respective intervals aforementioned.

To quantify the impact of these local motifs based on the B metal off center and Cs displacements into T and P networks, root mean square distance (RMSD) analysis was performed by taking the respective R networks as a reference for each chemical composition (Figure 4). RMSD was calculated through ArbAlign[48] protocol, which is based on the best overlap of a particular set of positions (Cs and B displaced) from a reference (Cs and B in the high symmetric R network). As previously evidenced by $g(r)$, all T networks present RMSD ~ 0.0 Å given the insignificant contributions for B off centering and Cs displacements of their respective sites. Conversely, one observes in P networks of $CsGeX_3$ compounds that Ge off centering is more pronounced than Sn in the $CsSnX_3$ corresponding network. Both $CsGeX_3$ and $CsSnX_3$ inorganic MHPs reveal

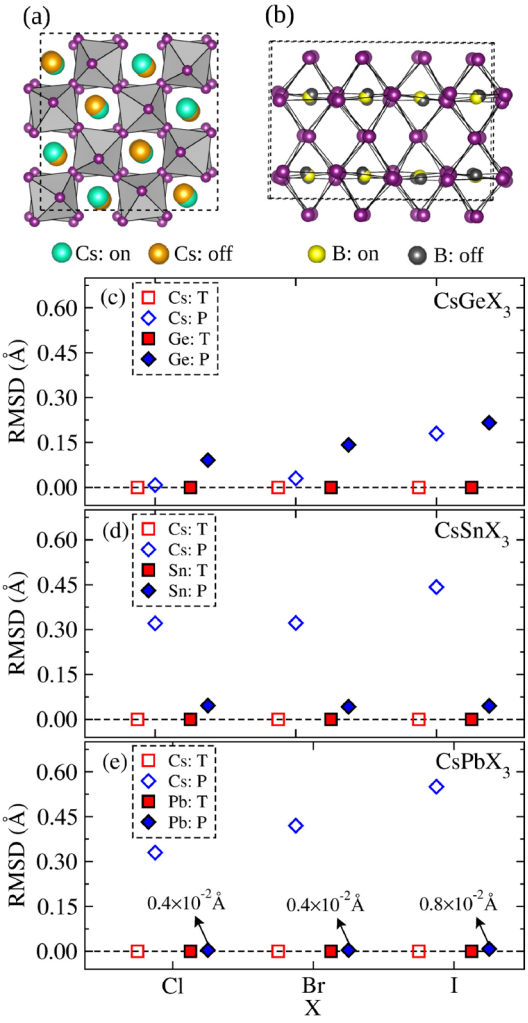

Figure 4. (a) Graphical representations of the displacements (off centering) of Cs and B species with respect to the R network (on centering). Quantification of B off centering and Cs displacements into (b) $CsGeX_3$, (c) $CsSnX_3$, and (d) $CsPbX_3$ inorganic MHPs by root mean square distance (RMSD) through ArbAlign[48] protocol for T and P networks.

the important role of the halogen dimension for the space availability in the cuboctahedral cavity, because the Cs displacements increase as the atomic size of X increases (Cl < Br < I).

The magnitude of the B metal displacements correlates inversely with the Ge < Sn < Pb sequence for metal sizes, given that larger atoms fill the volume inside octahedrons better throughout the metal size sequence. Thus, the RMSD for Pb is small in all $CsPbX_3$ (given RMSD order in 1×10^{-2} Å), leading to a Pb off centering secondary contribution by comparing with Cs displacements. At the same time, the RMSD increases for the Cl < Br < I as evidence of the halogen dimensions forming the cavity volume, consequently enhancing the inner space for the Cs mobility. Therefore, our insights show that the critical role of the chemical composition for structural motifs predominates in the polymorphic network formation. For instance, our previous investigation[36] revealed that the combination of metal off centering and the presence of intense SOC energies (as from Pb and I dominating the valence and conduction band edges) compose the recipe for the bulk Rashba splitting enhancement, which is crucial for increasing the charge carrier lifetimes.

Relative Energy of T and P Regarding R. To verify the thermodynamic feasibility of the T and P networks in each MHP composition with respect to their R analogs, we calculated the relative energy (E_{rel}) through $E_{rel}(T \text{ or } P) = [E_{P,T} - E_R]/N$, where $E_{P,T}$ is the total energy of the T (or P) network, E_R is the total energy of the R network, and N is the number of atoms into both supercells. The physical significance of E_{rel} is verifying the relative stability of the T and P networks concerning their R counterparts to analyze how the local structural contributions discussed in the previous section stabilize the former regarding the latter for a particular $CsBX_3$ composition. Figure 5 shows E_{rel} of the T and P network for $CsGeX_3$, $CsSnX_3$, and $CsPbX_3$ for all X halogens.

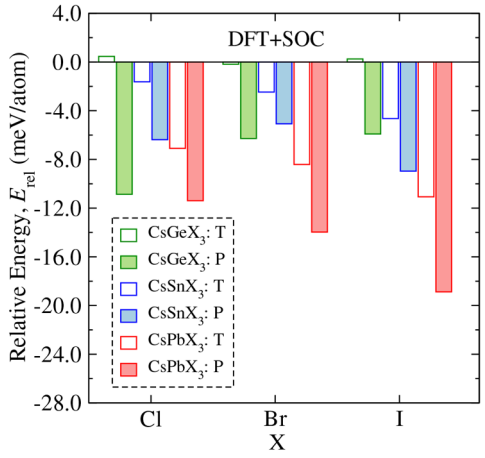

Figure 5. Relative energy calculated via DFT+SOC of the T and P networks calculated with respect to their R networks counterparts for $CsGeX_3$, $CsSnX_3$, and $CsPbX_3$ (X = Cl, Br, and I).

We found that P networks are greatly more stable than T and R for all inorganic MHP compositions, which indicates the important role of the structural degrees of freedom as local contributions, i.e., starting from R (monomorphic) and increasing the stability gradually through T (one local contribution) and going to P (set of local contributions) networks. Our results reveal the energetic role of local motif contributions into the structure through B metal off center displacements, octahedrons tilts, and Cs rearrangements on the polymorphic stability. This is evident when the stability magnitudes of T and P regarding R are compared, e.g., as for $CsGeX_3$ in which the T networks characterized by equatorial plane tilting are degenerated with high symmetry R given their $E_{rel} \sim 1$ meV/atom. Conversely, more favorable P $CsGeX_3$ networks present magnitude of E_{rel} decreasing in the Cl → Br → I sequence, which is due to the Ge metal off centering, Cs displacement contributions (as shown in Figure 4), and octahedral distortions (as shown in Figure 3 from the double $B-X^{(1)}$ distance) on the stabilization. Because Ge is 45.77% smaller than Cs,[46] it confers more compact cuboctahedral cavities for $CsGeX_3$. When the size of X decreases, although the distortions are smaller in magnitude for $CsGeCl_3$, they more pronouncedly affect this energy issue than in $CsGeI_3$, exactly because of the higher compactness of the ionic network for the former with respect to the latter.

In opposition to the $CsGeX_3$ MHPs, the relative stability of P (and T) regarding their respective R for $CsPbX_3$ networks increases in the Cl → Br → I sequence, highlighting the local motif contributions for the relative stability, as previously observed given the inclusion of Pb off centering contribution and Cs displacements for the P network because in modulus $E_{rel}(P) > E_{rel}(T)$. For $CsSnX_3$, $E_{rel}(T)$ presents the same tendency, which is expected because Sn is only 0.84% smaller than Pb. However, for the P network the stability regarding R increases from Br → Cl → I, which suggests that the Sn off centering energetic contribution is higher than from Cs displacements, so that RMSD(Cs) > RMSD(Sn).

Gap Energy with DFT-1/2+SOC. We employed a relativistic quasiparticle correction (named DFT 1/2) combined with SOC to calculate all the gap energies (E_g) for $CsGeX_3$, $CsSnX_3$, and $CsPbX_3$ (X = Cl, Br, or I) polymorphs (Figure 6). We provide outstanding gap energies values in agreement with experimental results. The collaborative effects of the local motifs contributing to the gap energies were investigated, comparing UC, R, T, and P network values with experimental gap energies reported from the literature. Under estimated results for DFT+SOC faced with the relativistic protocol are available in Supporting Information (Table S1) for all compositions and cell sizes. The DFT 1/2+SOC approach has been used with great success to predict the gap energies of hybrid perovskites.[35,36]

The effects of the octahedron break symmetry over the E_g value appear when the UC and R networks are compared. $CsGeX_3$ as UCs present high metal off centering (Table S2 in Supporting Information), which is completely suppressed in the symmetrical $CsSnX_3$ and $CsPbX_3$ systems. This explains E_g from $CsGeX_3$ as UC being overestimated with respect to the experiments (red bars in Figure 6), while being underestimated for the others. A second difference between the UC and R networks is the slight contraction of the lattice parameters for the R networks with respect to the UC, which leads to a gap energy closing in correlation with the lattice parameter differences (Figure 2) between them.

We found that our calculated E_g converge to the experimental values moving from R → T → P networks to all inorganic MHPs. The experimental gap energies of the $CsGeCl_3$,[22] $CsGeBr_3$,[22] $CsSnCl_3$,[49] and $CsPbBr_3$[52,53] are reported from the literature in a range of values, as depicted by the vertical lines in panels a, b, d, and h, respectively, whereas for the other ones, a single value was found. All R $CsBX_3$ networks have the most underestimated E_g with respect to the experiments; conversely, the tilts of neighbor octahedrons promote the E_g opening in all the T networks, which is due to the elongation of the B−X bond lengths in R → T. While the calculated values for $CsGeCl_3$ and $CsGeBr_3$ T networks reach the minima values from the experimental ranges (performed under high pressure, at 3.3 GPa for $CsGeCl_3$ and 1.2 GPa for $CsGeBr_3$)[22] with only a small opening regarding R networks, charts a and b, $CsPbBr_3$ has the second best E_g with underestimation of 5.3% only with octahedron tilt contributions. Furthermore, it is worth mentioning that, in general, this particular motif has less impact in $CsGeX_3$ in comparison with the $CsSnX_3$ and $CsPbX_3$ MHPs, which suggests that other contributions such as those in P networks must be considered.

E_g for the P networks reach outstanding values with respect to the experiments. For instance, while E_g values for $CsGeCl_3$, $CsGeBr_3$, $CsSnCl_3$, and $CsPbBr_3$ lie inside the experimental range, $CsSnBr_3$ (1.75 eV) and $CsPbI_3$ (1.73 eV) reach the same experimental value. The largest difference is for $CsGeI_3$ with E_g = 1.54 eV, which is only 5.52% lower than its experimental value. The E_g results suggest that all local motifs, such as octahedral tilts, B off centering, and Cs displacements (and gathered in the

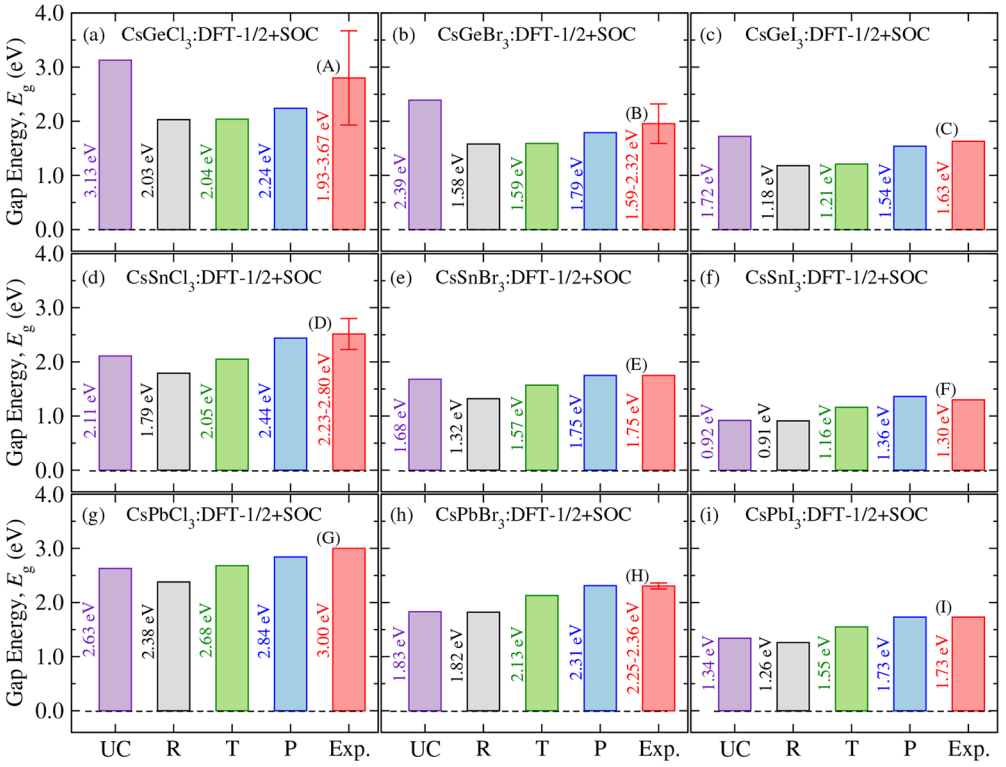

Figure 6. Gap energies (E_g) calculated for (a) $CsGeCl_3$, (b) $CsGeBr_3$, (c) $CsGeI_3$, (d) $CsSnCl_3$, (e) $CsSnBr_3$, (f) $CsSnI_3$, (g) $CsPbCl_3$, (h) $CsPbBr_3$, and (i) $CsPbI_3$ in the UC, R, T, and P networks. Experimental reference values are indicated by the red plots from refs (A and B) 22, (C) 18, (D) 49, (E) 50, 51, (F) 3, (G) 52, (H) 52, 53, and (I) 19.

P networks), contribute collectively to the gap energy opening. Even though in all inorganic MHPs the valence band maximum (VBM) consists of s and p orbitals from BX and the conduction band minimum (CBM) in p orbitals from B,[13,54−56] the strength of the SOC effect has shown an important factor for E_g when local distortions are present in the structure.[36]

We found that the metal SOC energies (E_{SOC}) play an important role for E_g (DFT 1/2+SOC), contributing to its improvement with respect to the experiments. Figure 7 (a) illustrates a scheme for the valence, which is composed mostly by p orbitals from X halogens, and conduction bands, composed mainly by p orbitals from B metals. As an effect of the local motif contributions and an additional contribution of the E_{SOC} magnitude for the metals, the gap opening follows the $E_g^R \rightarrow E_g^T \rightarrow E_g^P$ sequence where the last one is in outstanding agreement with experiments. Panel b shows the intervals where E_{SOC} for Ge, Sn, and Pb metals appear in 17−23 meV/atom, 113−140 meV/atom, and 900−1200 meV/atom intervals, respectively, for all R, T, and P networks; numeric values for all chemical species, ionic networks (UC, R, T, and P), and calculations involving standard DFT (i.e., without SOC), DFT +SOC, and DFT 1/2+SOC are available in Supporting Information (Tables S1 and S4), from which the impact of structural changes and relativistic effects on the gap energies can be seen in detail. Because B off centering is the principal difference from T to P network, one observes that the correlation between SOC magnitude and low symmetry motif reveals an improvement of E_g. For $CsPbX_3$ MHPs, Pb metals are less off centering than B metals in $CsGeX_3$ and $CsSnX_3$, as depicted by RMSD in Figure 4; however, the small displacement is enough to enlarge the strong SOC effect from Pb on the E_g results.

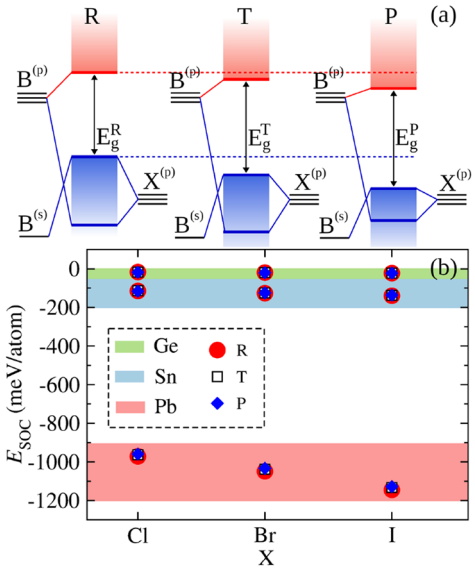

Figure 7. (a) Schematic energy level diagram of the VBM and CBM composed of $B^{(s,p)}$ and $X^{(p)}$ (s and p orbitals) and affected given the local motif contributions, leading to the gap opening from the $E_g^R \rightarrow E_g^T \rightarrow E_g^P$ sequence. (b) Spin−orbit energies for the B metals in the R, T, and P networks for $CsGeX_3$, $CsSnX_3$, and $CsPbX_3$ (X = Cl, Br, and I).

Optical Absorption Coefficient. Aiming to provide a deeper description of the inorganic $CsBX_3$ MHPs, we compared the absorption coefficients ($\alpha(\omega)$) among the R, T, and P networks, as shown in Figure 8. One observes in all MHP compositions that the absorption follows the behavior of the gap, and the $\alpha(\omega)$ onset tends to blueshift toward the R → T →

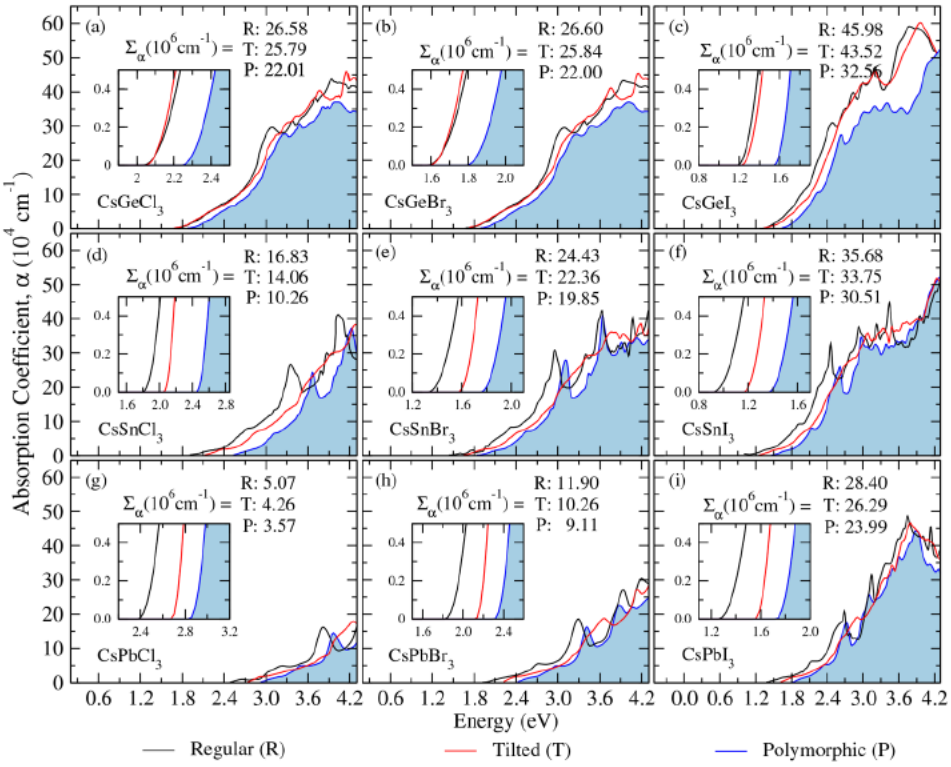

Figure 8. Absorption coefficients $\alpha(\omega)$ calculated via DFT 1/2+SOC for all inorganic MHPs (a) $CsGeCl_3$, (b) $CsGeBr_3$, (c) $CsGeI_3$, (d) $CsSnCl_3$, (e) $CsSnBr_3$, (f) $CsSnI_3$, (g) $CsPbCl_3$, (h) $CsPbBr_3$, and (i) $CsPbI_3$ in R, T, and P. Total absorbance ($\sum_\alpha$) values are depicted for the 0.0−4.2 eV interval.

P sequence networks. On the other hand, considering a given network, the halogen sequence for a particular B correlates the gap opening with the increase in the B−X electronegativity difference, as observed from the Pauling electronegativities for the Pb (2.33), Sn (1.96), and Ge (2.01) metals and Cl (3.16), Br (2.96), and I (2.66) halogens.[57,58]

As highlighted through the small charts, all the optical gaps tend to coincide with their respective fundamental gaps, which indicates that there are no prohibited transitions near the band edges for all systems. Nevertheless, it is worth mentioning the reduction in $\alpha(\omega)$ transitions beyond the CBM (in photo energies higher than gap energies) from the R → T → P structural changes in all MHPs, as depicted by the total absorbance ($\sum_\alpha$ for the 0.0−4.2 eV interval). Conversely, our results for $\sum_\alpha$ suggest that the collective effects involving all local structural motifs play an important role in the optical properties.

We found a strong correlation between chemical composition (halogen and metal) and polymorphic networks concerning a high $\sum_\alpha$ and minimum E_g, as depicted in Figure 9, by joining composition and electronic parameters. From the metal perspective, one observes a reduction of $\sum_\alpha$ for $CsBI_3$ → $CsBCl_3$ at around 32%, 66%, and 85% for B = Ge, Sn, and Pb, respectively. However, when keeping a given halogen and changing the metal, $\sum_\alpha$ reduces less, especially for I, so that for $CsGeX_3$ → $CsPbX_3$, $\sum_\alpha$ is around 83%, 58%, and 26% for X = Cl, Br, and I, respectively. Therefore, our results indicate that to avoid a pronounced $\sum_\alpha$ suppression, it is most indicated to proceed with the Pb → Ge replacement in $CsBI_3$ MPHs, leading to the $CsSnI_3$, $CsGeI_3$, $CsSnBr_3$, or $CsGeBr_3$ as green alternative aiming materials with optical and gap energy values comparative to the most explored $CsPbI_3$.

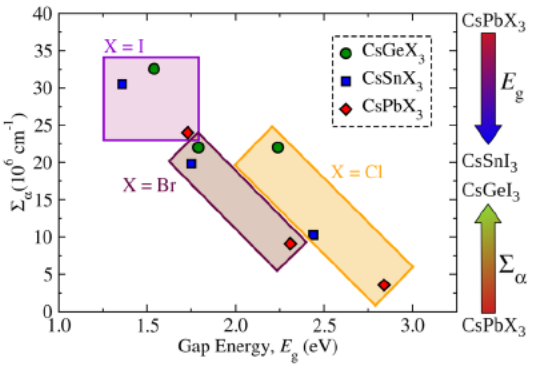

Figure 9. Correlation among total absorption energies ($\sum_\alpha$), gap energies (E_g), and compositions for polymorphic $2\sqrt{2} \times 2\sqrt{2} \times 2$ networks of all MHPs, i.e., $CsBX_3$ with B = Ge, Sn, or Pb, and X = Cl, Br, or I.

4. SUMMARY

We presented a comprehensive investigation about the polymorphic nature of all inorganic $CsBX_3$ (B = Ge, Sn, Pb, and X = Cl, Br, I) cubic perovskites, analyzing in detail the influence of polymorphic motifs over the energy stability and optoelectronic properties, such as gap energies and optical absorption coefficients. Our results indicate that a set of local motifs such as distortions on the octahedrons, relative tiltings, Cs displacement, and metal off centering networks play a crucial role in the stability and optoelectronic properties of inorganic MHPs. We showed that the increase in spin−orbit coupling (SOC) energy throughout the Ge → Sn → Pb sequence over the aforementioned local motifs directly affects their thermodynamic stability and electronic properties. At the same time, the stability correlates with the SOC energy increase from the

halogens in the Cl → Br → I sequence for $CsSnX_3$ and $CsPbX_3$, whereas for the $CsGeX_3$ series, it is the opposite sequence for the halogens, given the role of the Ge small size (and small SOC contributions) on the structure distortion. By combining the low cost DFT 1/2 relativistic quasiparticle correction with SOC, we overcame the limitations of DFT to calculate the gap energies to obtain outstanding values concerning the exper imental reports, showing that the experimental measurement is (actually) an average from structural local motif contributions. The polymorphic nature of cubic perovskites leads to a blue shift in the absorption onset of their UV−vis spectra in correlation with the gap opening, given that any prohibited transition was found. Furthermore, we showed a perspective of chemical design to avoid a pronounced $\sum_\alpha$ suppression combined with gap energy closing especially prioritizing the replacement of toxic Pb in green alternatives such as $CsSnI_3$, $CsGeI_3$, $CsSnBr_3$, or $CsGeBr_3$. Therefore, our results open a potential perspective through a deeper understanding of all inorganic metal halide perovskites concerning the design of solar cell devices.

ASSOCIATED CONTENT

Supporting Information

The Supporting Information is available free of charge at https://pubs.acs.org/doi/10.1021/acs.jpcc.1c08923.

Details of the quasiparticle correction (DFT 1/2) methodology; optimization of CUT parameter; models of local structural contributions for the polymorphic networks; gap energies calculated through DFT, DFT +SOC, and DFT 1/2+SOC; structure parameters; percent deviation of the calculated lattice parameters with respect to the experiments; spin−orbit coupling energies for all chemical species in the ABX_3; and general Cartesian representation for unit cell, $\sqrt{2} \times \sqrt{2} \times 2$ (T and R polymorphic networks), and $2\sqrt{2} \times 2\sqrt{2} \times 2$ (T and R polymorphic networks) (PDF)

AUTHOR INFORMATION

Corresponding Authors

Luis Octavio de Araujo − *Chemistry Department, Federal University of Paraná, 81531 980 Curitiba, Brazil*; Email: luisaraujo@ufpr.br

Celso R. C. Rêgo − *Karlsruhe Institute of Technology (KIT), Institute of Nanotechnology Hermann von Helmholtz Platz, 76344 Eggenstein Leopoldshafen, Germany*; orcid.org/0000 0003 1861 2438; Email: celso.rego@kit.edu

W. Wenzel − *Karlsruhe Institute of Technology (KIT), Institute of Nanotechnology Hermann von Helmholtz Platz, 76344 Eggenstein Leopoldshafen, Germany*; orcid.org/0000 0001 9487 4689; Email: wolfgang.wenzel@kit.edu

Fernando P. Sabino − *Center for Natural and Human Sciences, Federal University of ABC, 09210 580 Santo André, SP, Brazil*; Email: fernandopsabino@yahoo.com.br

Diego Guedes Sobrinho − *Chemistry Department, Federal University of Paraná, 81531 980 Curitiba, Brazil*; orcid.org/0000 0002 3313 2822; Email: guedessobrinho@ufpr.br

Notes

The authors declare no competing financial interest.

ACKNOWLEDGMENTS

The authors thank the Yemoja Computer at CIMATEC SENAI (Salvador − BA) and Laboratório Central de Processamento de Alto Desempenho (LCPAD) financed by FINEP through CT INFRA/UFPR projects, both in Brazil for the support to perform the electronic structure calculations. Luis O. de Araujo thanks Coordenação de Aperfeiçoamento de Pessoal de Nível Superior (CAPES) for funding. Fernando P. Sabino thanks São Paulo Research Foundation (FAPESP) for grant 2019/21656 8. W. Wenzel acknowledges the financial support by Deutsche Forschungsgemeinschaft (DFG, German Research Foundation) through project WE 1863/29 1. W. Wenzel and Celso R. C. Rêgo thank the German Federal Ministry of Education and Research (BMBF) for financial support of the project Innovation Platform MaterialDigital (www.materialdigital.de) through project funding FKZ no. 13XP5094A.

REFERENCES

(1) Jeong, J.; Kim, M.; Seo, J.; Lu, H.; Ahlawat, P.; Mishra, A.; Yang, Y.; Hope, M. A.; Eickemeyer, F. T.; Kim, M.; et al. Pseudo Halide Anion Engineering for α $FAPbI_3$ Perovskite Solar Cells. *Nature* **2021**, *592*, 381−385.

(2) Zhang, J.; Hodes, G.; Jin, Z.; Liu, S. F. All Inorganic $CsPbX_3$ Perovskite Solar Cells: Progress and Prospects. *Angew. Chem., Int. Ed.* **2019**, *58*, 15596−15618.

(3) Stoumpos, C. C.; Malliakas, C. D.; Kanatzidis, M. G. Semi conducting Tin and Lead Iodide Perovskites with Organic Cations: Phase Transitions, High Mobilities, and Near Infrared Photolumines cent Properties. *Inorg. Chem.* **2013**, *52*, 9019−9038.

(4) Noel, N. K.; Stranks, S. D.; Abate, A.; Wehrenfennig, C.; Guarnera, S.; Haghighirad, A. A.; Sadhanala, A.; Eperon, G. E.; Pathak, S. K.; Johnston, M. B.; et al. Lead free Organic Inorganic Tin Halide Perovskites for Photovoltaic Applications. *Energy Environ. Sci.* **2014**, *7*, 3061−3068.

(5) Pecunia, V.; Occhipinti, L. G.; Chakraborty, A.; Pan, Y.; Peng, Y. Lead Free Halide Perovskite Photovoltaics: Challenges, Open Questions, and Opportunities. *APL Mater.* **2020**, *8*, 100901.

(6) Zheng, F.; Tan, L. Z.; Liu, S.; Rappe, A. M. Rashba Spin Orbit Coupling Enhanced Carrier Lifetime in $CH_3NH_3PbI_3$. *Nano Lett.* **2015**, *15*, 7794−7800.

(7) Ju, M.; Chen, M.; Zhou, Y.; Dai, J.; Ma, L.; Padture, N. P.; Zeng, X. C. Toward Eco Friendly and Stable Perovskite Materials for Photo voltaics. *Joule* **2018**, *2*, 1231−1241.

(8) Yang, R. X.; Skelton, J. M.; da Silva, E. L.; Frost, J. M.; Walsh, A. Spontaneous Octahedral Tilting in the Cubic Inorganic Cesium Halide Perovskites $CsSnX_3$ and $CsPbX_3$ (X = F, Cl, Br, I). *J. Phys. Chem. Lett.* **2017**, *8*, 4720−4726.

(9) Zhao, X.; Dalpian, G. M.; Wang, Z.; Zunger, A. Polymorphous Nature of Cubic Halide Perovskites. *Phys. Rev. B* **2020**, *101*, 155137.

(10) Dalpian, G. M.; Zhao, X.; Kazmerski, L.; Zunger, A. Formation and Composition Dependent Properties of Alloys of Cubic Halide Perovskites. *Chem. Mater.* **2019**, *31*, 2497−2506.

(11) Dias, A. C.; Lima, M. P.; Da Silva, J. L. F. Role of Structural Phases and Octahedra Distortions in the Optoelectronic and Excitonic Properties of $CsGeX_3$ (X = Cl, Br, I) Perovskites. *J. Phys. Chem. C* **2021**, *125*, 19142−19155.

(12) Borriello, I.; Cantele, G.; Ninno, D. *Ab initio* Investigation of Hybrid Organic Inorganic Perovskites Based on Tin Halides. *Phys. Rev. B* **2008**, *77*, 235214.

(13) Huang, L.; Lambrecht, W. R. L. Electronic Band Structure, Phonons, and Exciton Binding Energies of Halide Perovskites $CsSnCl_3$, $CsSnBr_3$, and $CsSnI_3$. *Phys. Rev. B* **2013**, *88*, 165203.

(14) Manser, J. S.; Christians, J. A.; Kamat, P. V. Intriguing Optoelectronic Properties of Metal Halide Perovskites. *Chem. Rev.* **2016**, *116*, 12956−13008.

(15) Ming, W.; Shi, H.; Du, M. Large Dielectric Constant, High Acceptor Density, and Deep Electron Traps in Perovskite Solar Cell Material $CsGeI_3$. *J. Mater. Chem. A* **2016**, *4*, 13852−13858.
(16) Liu, B.; Long, M.; Cai, M.; Yang, J. Influence of the Number of Layers on Ultrathin $CsSnI_3$ Perovskite: from Electronic Structure to Carrier Mobility. *J. Phys. D: Appl. Phys.* **2018**, *51*, 105101.
(17) Fadla, M. A.; Bentria, B.; Dahame, T.; Benghia, A. First Principles Investigation on the Stability and Material Properties of All Inorganic Cesium Lead Iodide Perovskites $CsPbI_3$ Polymorphs. *Physica B Condens. Matter* **2020**, *585*, 412118.
(18) Krishnamoorthy, T.; Ding, H.; Yan, C.; Leong, W. L.; Baikie, T.; Zhang, Z.; Sherburne, M.; Li, S.; Asta, M.; Mathews, N.; et al. Lead Free Germanium Iodide Perovskite Materials for Photovoltaic Applications. *J. Mater. Chem. A* **2015**, *3*, 23829−23832.
(19) Sanehira, E. M.; Marshall, A. R.; Christians, J. A.; Harvey, S. P.; Ciesielski, P. N.; Wheeler, L. M.; Schulz, P.; Lin, L. Y.; Beard, M. C.; Luther, J. M. Enhanced Mobility $CsPbI_3$ Quantum Dot Arrays for Record Efficiency, High Voltage Photovoltaic Cells. *Sci. Adv.* **2017**, *3*, eaao4204.
(20) Heyd, J.; Scuseria, G. E.; Ernzerhof, M. Hybrid Functionals Based on a Screened Coulomb Potential. *J. Chem. Phys.* **2003**, *118*, 8207−8215.
(21) Krukau, A. V.; Vydrov, O. A.; Izmaylov, A. F.; Scuseria, G. E. Influence of the Exchange Screening Parameter on the Performance of Screened Hybrid Functionals. *J. Chem. Phys.* **2006**, *125*, 224106.
(22) Seo, D.; Gupta, N.; Whangbo, M.; Hillebrecht, H.; Thiele, G. Pressure Induced Changes in the Structure and Band Gap of $CsGeX_3$ (X = Cl, Br) Studied by Electronic Band Structure Calculations. *Inorg. Chem.* **1998**, *37*, 407−410.
(23) Park, J.; Jung, J.; Lee, S. Cost Effective High Throughput Calculation Based on Hybrid Density Functional Theory: Application to Cubic, Double, and Vacancy Ordered Halide Perovskites. *J. Phys. Chem. Lett.* **2021**, *12*, 7885−7891.
(24) van Schilfgaarde, M.; Kotani, T.; Faleev, S. Quasiparticle Self Consistent GW Theory. *Phys. Rev. Lett.* **2006**, *96*, 226402.
(25) Tao, S. X.; Cao, X.; Bobbert, P. A. Accurate and Efficient Band Gap Predictions of Metal Halide Perovskites Using the DFT 1/2 Method: GW Accuracy with DFT Expense. *Sci. Rep.* **2017**, *7*, 14386.
(26) Ferreira, L. G.; Marques, M.; Teles, L. K. Approximation to Density Functional Theory for the Calculation of Band Gaps of Semiconductors. *Phys. Rev. B* **2008**, *78*, 125116.
(27) Hohenberg, P.; Kohn, W. Inhomogeneous Electron Gas. *Phys. Rev.* **1964**, *136*, B864−B871.
(28) Kohn, W.; Sham, L. J. Self Consistent Equations Including Exchange and Correlation Effects. *Phys. Rev.* **1965**, *140*, A1133−A1138.
(29) Perdew, J. P.; Burke, K.; Ernzerhof, M. Generalized Gradient Approximation Made Simple. *Phys. Rev. Lett.* **1996**, *77*, 3865−3868.
(30) Kresse, G.; Hafner, J. *Ab Initio* Molecular Dynamics for Open Shell Transition Metals. *Phys. Rev. B* **1993**, *48*, 13115−13118.
(31) Kresse, G.; Furthmüller, J. Efficient Iterative Schemes for *Ab Initio* Total Energy Calculations Using a Plane Wave Basis Set. *Phys. Rev. B* **1996**, *54*, 11169−11186.
(32) Blöchl, P. E. Projector Augmented Wave Method. *Phys. Rev. B* **1994**, *50*, 17953−17979.
(33) Slater, J. C.; Johnson, K. H. Self Consistent Field X−α Cluster Method for Polyatomic Molecules and Solids. *Phys. Rev. B* **1972**, *5*, 844−853.
(34) Ferreira, L. G.; Marques, M.; Teles, L. K. Slater Half Occupation Technique Revisited: The LDA 1/2 and GGA 1/2 Approaches for Atomic Ionization Energies and Band Gaps in Semiconductors. *AIP Adv.* **2011**, *1*, 032119.
(35) Guedes Sobrinho, D.; Guilhon, I.; Marques, M.; Teles, L. K. Relativistic DFT 1/2 Calculations Combined with a Statistical Approach for Electronic and Optical Properties of Mixed Metal Hybrid Perovskites. *J. Phys. Chem. Lett.* **2019**, *10*, 4245−4251.
(36) de Araujo, L. O.; Sabino, F. P.; Rêgo, C. R. C.; Guedes Sobrinho, D. Bulk Rashba Effect Splitting and Suppression in Polymorphs of Metal Iodine Perovskites. *J. Phys. Chem. Lett.* **2021**, *12*, 7245−7251.
(37) Gajdoš, M.; Hummer, K.; Kresse, G.; Furthmüller, J.; Bechstedt, F. Linear Optical Properties in the Projector Augmented Wave Methodology. *Phys. Rev. B* **2006**, *73*, 045112.
(38) Hu, B. Y. Kramers Kronig in two lines. *Am. J. Phys.* **1989**, *57*, 821−821.
(39) Rêgo, C. R. C. KIT Workflows/DFT VASP: DFT VASP. https://github.com/KIT Workflows/DFT VASP (accessed Sep 12, 2021).
(40) Schaarschmidt, J.; Yuan, J.; Strunk, T.; Kondov, I.; Huber, S. P.; Pizzi, G.; Kahle, L.; Bolle, F. T.; Castelli, I. E.; Vegge, T.; et al. Workflow Engineering in Materials Design within the BATTERY 2030+ Project. *Adv. Energy Mater.* **2021**, 2102638.
(41) Jellicoe, T. C.; Richter, J. M.; Glass, H. F. J.; Tabachnyk, M.; Brady, R.; Dutton, S. E.; Rao, A.; Friend, R. H.; Credgington, D.; Greenham, N. C.; et al. Synthesis and Optical Properties of Lead Free Cesium Tin Halide Perovskite Nanocrystals. *J. Am. Chem. Soc.* **2016**, *138*, 2941−2944.
(42) Yamada, K.; Funabiki, S.; Horimoto, H.; Matsui, T.; Okuda, T.; Ichiba, S. Structural Phase Transitions of the Polymorphs of $CsSnI_3$ by Means of Rietveld Analysis of the X Ray Diffraction. *Chem. Lett.* **1991**, *20*, 801−804.
(43) Zheng, J.; Huan, C. H. A.; Wee, A. T. S.; Kuok, M. H. Electronic Properties of $CsSnBr_3$: Studies by Experiment and Theory. *Surf. Interface Anal.* **1999**, *28*, 81−83.
(44) Møller, C. K. Crystal Structure and Photoconductivity of Cæsium Plumbohalides. *Nature* **1958**, *182*, 1436−1436.
(45) Sharma, S.; Weiden, N.; Weiss, A. Phase Diagrams of Quasibinary Systems of the Type: ABX_3−$A'BX_3$; ABX_3−$AB'X_3$, and ABX_3−ABX'_3. *Z. Phys. Chem.* **1992**, *175*, 63−80.
(46) Kittel, C. *Introduction to Solid State Physics*, 8th ed.; John Wiley & Sons, Inc.: New York, 2004.
(47) Glazer, A. M. The Classification of Tilted Octahedra in Perovskites. *Acta Crystallogr., Sect. B: Struct. Crystallogr. Cryst. Chem.* **1972**, *28*, 3384−3392.
(48) Temelso, B.; Mabey, J. M.; Kubota, T.; Appiah Padi, N.; Shields, G. C. ArbAlign: A Tool for Optimal Alignment of Arbitrarily Ordered Isomers Using the Kuhn Munkres Algorithm. *J. Chem. Inf. Model.* **2017**, *57*, 1045−1054.
(49) Voloshinovskii, A. S.; Myagkota, S. V.; Pidzyrailo, N. S.; Tokarivskii, M. V. Luminescence and Structural Transformations of $CsSnCl_3$ Crystals. *J. Appl. Spectrosc.* **1994**, *60*, 226−228.
(50) Sabba, D.; Mulmudi, H. K.; Prabhakar, R. R.; Krishnamoorthy, T.; Baikie, T.; Boix, P. P.; Mhaisalkar, S.; Mathews, N. Impact of Anionic Br^- Substitution on Open Circuit Voltage in Lead Free Perovskite ($CsSnI_{3-x}Br_x$) Solar Cells. *J. Phys. Chem. C* **2015**, *119*, 1763−1767.
(51) Kar, M.; Korzdorfer, T. Computational High Throughput Screening of Inorganic Cation Based Halide Perovskites for Perovskite Only Tandem Solar Cells. *Mater. Res. Express* **2020**, *7*, 055502.
(52) Ahmad, M.; Rehman, G.; Ali, L.; Shafiq, M.; Iqbal, R.; Ahmad, R.; Khan, T.; Jalali Asadabadi, S.; Maqbool, M.; Ahmad, I. Structural, Electronic and Optical Properties of $CsPbX_3$ (X = Cl, Br, I) for Energy Storage and Hybrid Solar Cell Applications. *J. Alloys Compd.* **2017**, *705*, 828−839.
(53) Thapa, S.; Bhardwaj, K.; Basel, S.; Pradhan, S.; Eling, C. J.; Adawi, A. M.; Bouillard, J. G.; Stasiuk, G. J.; Reiss, P.; Pariyar, A.; et al. Long Term Ambient Air Stable Cubic $CsPbBr_3$ Perovskite Quantum Dots Using Molecular Bromine. *Nanoscale Adv.* **2019**, *1*, 3388−3391.
(54) Rahaman, M. Z.; Akther Hossain, A. K. M. Effect of Metal Doping on the Visible Light Absorption, Electronic Structure and Mechanical Properties of Non Toxic Metal Halide $CsGeCl_3$. *RSC Adv.* **2018**, *8*, 33010−33018.
(55) Liu, D.; Li, Q.; Jing, H.; Wu, K. Pressure Induced Effects in the Inorganic Halide Perovskite $CsGeI_3$. *RSC Adv.* **2019**, *9*, 3279−3284.
(56) Xu, S.; Libanori, A.; Luo, G.; Chen, J. Engineering Bandgap of $CsPbI_3$ Over 1.7 eV with Enhanced Stability and Transport Properties. *IScience* **2021**, *24*, 102235.
(57) Pauling, L. *The Nature of the Chemical Bond*; Cornell University Press: Ithaca, 1960.

(58) Allred, A. L. Electronegativity Values from Thermochemical Data. *J. Inorg. Nucl. Chem.* **1961**, *17*, 215−221.